Zexun Wei
First Institute of Oceanography, SOA
6 Xian-xia-ling Road, Hi-Tech Industrial Park
Qingdao 266061, P. R. China
March 10, 2016

Dear Editor:

We are truly grateful to you and to the reviewers' constructive comments and thoughtful suggestions for our manuscript entitled "*Tidal elevation, current and energy flux in the area between the South China Sea and Java Sea*". The valuable comments certainly improve the paper. We have carefully revised the original manuscript according to these comments and suggestions. All changes made to the text are in "track-changes" mode.

Below you will find our point-by-point responses to the reviewers' comments. Thank you for the efforts and time given to this manuscript. Hopefully we have addressed all the concerns.

Sincerely,

Zexun Wei

Note: **The reviewers' comments are typed in blue color, while our responses are in black.**

Part A: Responses to anonymous Referee #1

I recommend this OSD to be published, since the observation and analysis from SITE project will be of good importance to numerical modeling of SCS and Java Sea

Reply:
Thanks for your positive evaluation.

Part B: Responses to anonymous Referee #2

This is a well prepared paper. The main message of the paper on the tidal dynamics in the area between the South China Sea and the Java Sea is clear. Since this region is commonly chosen as the open boundary in the numerical model of the SCS, the results shown in the paper are important and ready for immediate application. Below are two specific comments for the paper.

Reply:
Thanks for your positive evaluation.

1. First, in the results section, the authors may need describe their harmonic analysis method in details. Since it is a trivial work to extract the harmonic constants of the eight tidal constituents M2, S2, N2, K2, K1, P1, O1, Q1 in Foreman or Pawlowicz's program, it is not clear why the harmonic constants of P1 and K2 in the current method has to be inferred indirectly..

Reply:
In the text we have added "**According to Rayleigh criterion, to separate P_1 from K_1 and K_2 from S_2 reqires 182.6 days (e. g., Pugh, 1987, p.113), thus**".
In the references we added "**Pugh, D.T., 1987. Tides, Surges, and Mean Sea Level. John Wiley & Sons Ltd, 472 pp**".

2. Second, in the discussion section, the comparisons between the observational and the four global tidal model results are very ingesting. It shows that not a single model could produce an optimal solution for tidal prediction in this area. However it is not very clear what causes the inconsistent behaviors among the tidal models and how this could guide one to determine the tidal boundary conditions in a model. Since such a topic may attract a wide audience, this is the aspect which should be emphasized and is expected to improve the paper significantly.

Reply:

These four global ocean tide models were developed on the basis of satellite altimeter data, mostly TOPEX/Poseidon and Jason1/2 data. However the ground tracks of TOPEX/Poseidon and Jason-1/2 are coarse and altimeter measurement are relatively not accurate in shallow waters, these are likely the sources of the difference between models and observations. The following table (it has been attached to Table A1) lists the average deviations of five stations between four tidal models and observations. It shows that DTU10 is the best one in the area between the South China Sea and Java Sea, due to use of more satellites and longer altimeter measurements. Moreover, DTU10 has the highest resolution (0.125 by 0.125 degree) among these four tide models. If the open boundary of a tidal model is located in the area between the South China Sea and Java Sea, DTU10 is the best choice for deriving open boundary condition.

Average deviations of five stations between existing tidal models and observations (in cm)

	K_1	O_1	M_2	S_2
TPXO7.2	8.10	4.74	3.06	2.84
GOT00.2	7.42	5.58	1.86	2.56
NAO.99b	6.68	5.50	3.2	5.28
DTU10	5.32	3.76	1.02	2.52

Part C: Responses to Editor (N. C. Wells)

This is a very good paper and should be published in Ocean Sciences.

Reply:
Thanks for your positive evaluation.

1. There wasn’t any description and discussion of how a current profiles were obtained from top to bottom. Wind driven influences may have contaminated the data and what about the lower frictional layer? Were these things ignored, if so it should be said. Have you assumed this is barotropic and why?

Reply:
In response to your first concern we have added “**The vertical bin size of ADCP measurements are 1 m for Station A1 and 2 m for other stations.**” to the text to describe vertical sampling of the current profiles, and added a new column to Table 1 to show the bin size at each observational station.

Table 1. Locations, water depths, and ADCP bin sizes of the observational stations.

Station	Longitude	Latitude	Depth (m)	Bin size (m)
A1	106°50.1' E	1°40.0' S	36.6	1
A2	107°59.2' E	1°05.5' S	48.0	2
B1	107°09.6' E	2°46.8' S	44.2	2

B2	108°15.0' E	2°17.0' S	42.8	2
B3	108°33.0' E	1°54.9' S	49.0	2

In response to your second concern the vertical distributions of tidal current ellipses of constituents K_1, O_1, Q_1, M_2, S_2, and N_2 have been added to Section 3.2, which are shown below. We can see that there are little vertical changes in the ellipses for all constituents at all stations, except for the top layer, where the currents suffer strong disturbances due to winds, at some stations for some constituents. This vertical uniformity indicates that the tidal currents are basically of barotropic nature at all stations. Thus, we only use vertically averaged currents to reveal the characteristics of tidal currents in this study.

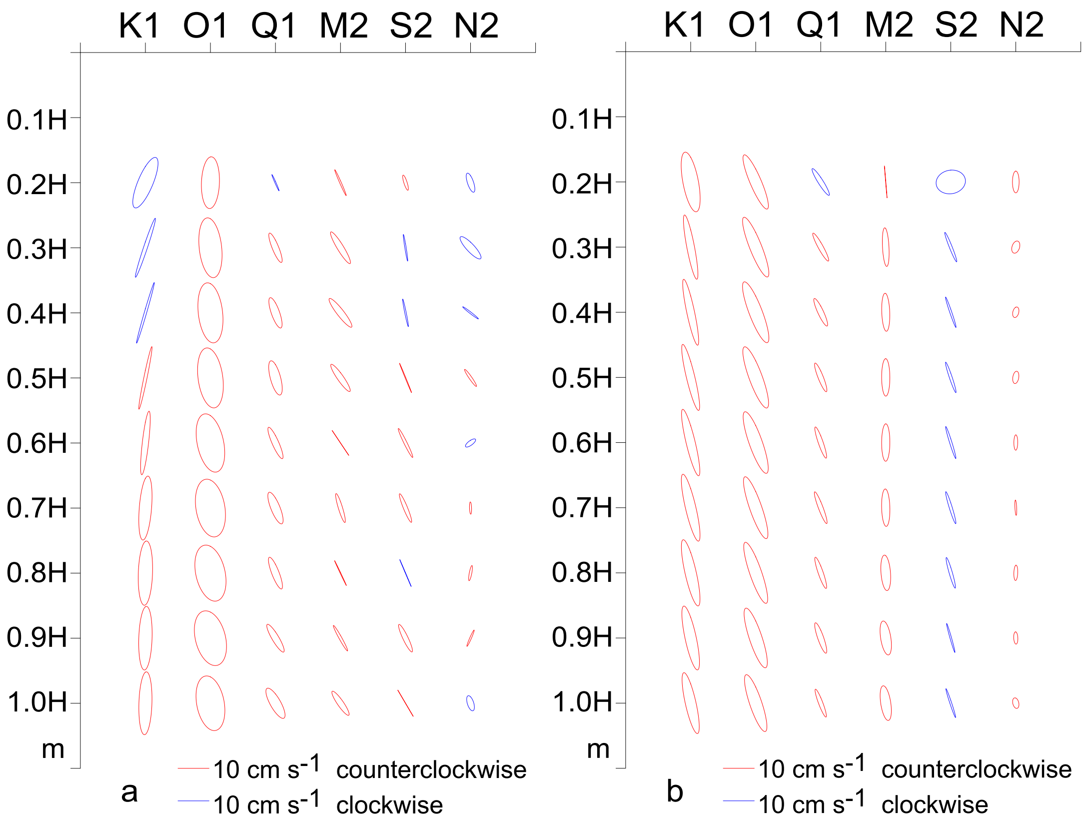

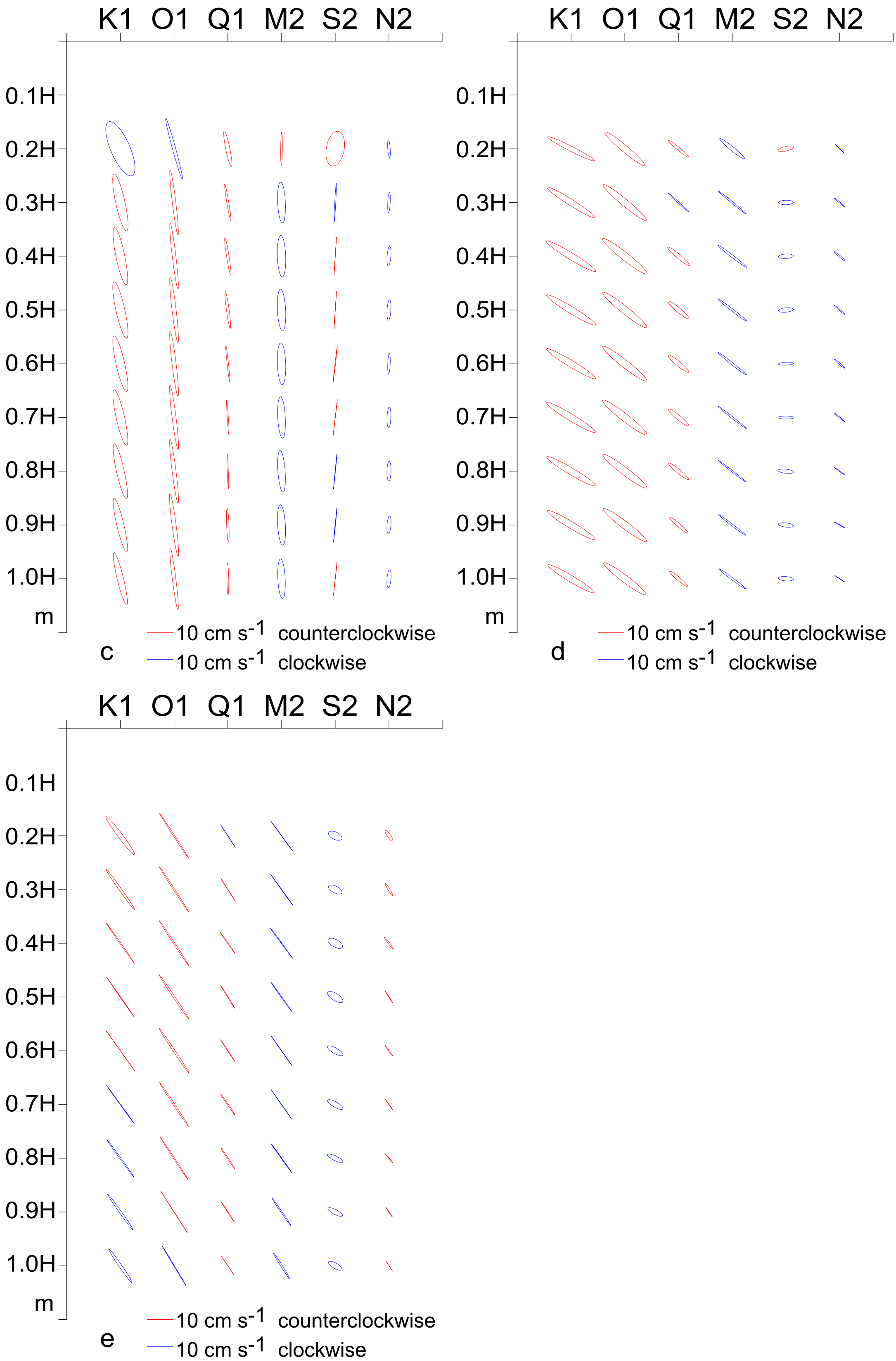

Fig. 2. The vertical distributions of current ellipses of tides constituents K_1, O_1, Q_1, M_2, S_2, and N_2 at Stations A1(a), A2(b), B1(c), B2(d) and B3(e)

2. Section 3.4 why have you done this analysis in this section if you are not going to show the co-tidal charts? If it is not relevant why do it? You could put a selection of the co-tidal charts in an appendix. I certainly would have liked to see them.

<u>Reply</u>:

In response to this comment the co-tidal charts based on DTU10 model have been added to Appendix. For K_1, the tidal waves from the SCS and the JS meet in the study area. For O_1, the tidal wave propagates from the SCS to the JS. For M_2, the tidal wave propagates clockwise around the Belitung Island. For S_2, the tidal wave also propagates clockwise around the Belitung Island, and one clockwise amphidromic system exists near Station A1. K_1 has the largest amplitude (exceeding 0.6 m near the Bangka Island), and then the next is O_1, the amplitudes of M_2 and S_2 are significantly smaller.

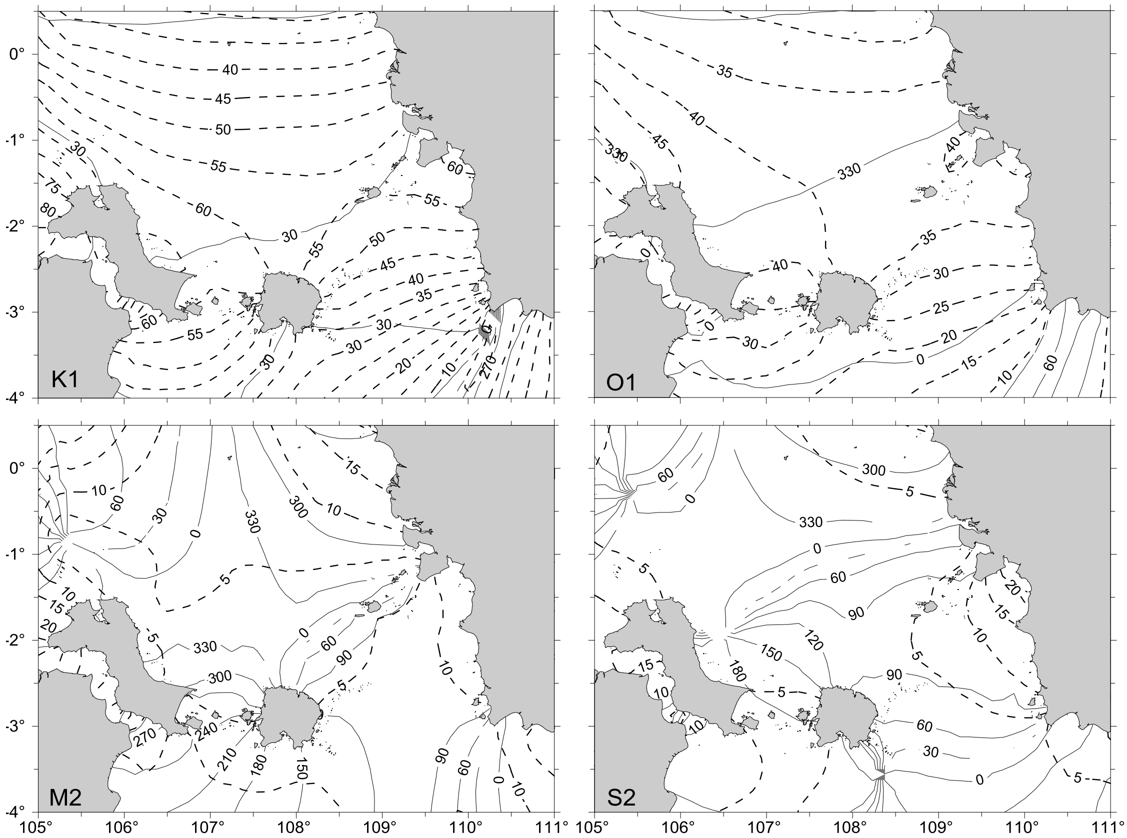

Co-tidal charts for K_1, O_1, M_2 and S_2 based on DTU10

Dashed line: amplitude (cm), solid line: phase-lag (°)

3. Specific Comments

P3 line 9 add “an” before “inversion”

<u>Reply</u>: Added as suggested.

P4 line 7-8, even the satellite....into the models. Phrase doesn’t make sense. Suggest... even when the satellite altimeter data has been assimilated into models.

<u>Reply</u>: Revised as suggested.

P4 line 17 Remove inverted commas from the word “is” in text.
Reply: Revised as suggested.

P4 line 19 Prefix last phrase by “Finally a summary. . .
Reply: Added as suggested.

P12 Line 15 Please use” anti-nodal” not “loop” at the above locations in the script. It is not used in the scientific community in the U.K.
Reply: The usage of “loop” is common in the US (see NOAA’s “Tide and Current Glossary”, which is available in NOAA’s website, initially written by Paul Schureman). However, it is truly more appropriate to use “anti-nodal” instead of “loop” in our paper which is submitted to Ocean Science, an European journal. Thus we have changed “loop” to “anti-nodal” at all places in the revised manuscript.

author's change list

page 2 line 17, page 3 line 22, page 7 line 2, page 12 line 15, “loop” changed to “anti-nodal”.

page 3 line 9, add “an” before “inversion”.

page 4 line 8, add “when” after “even”.

page 4 line 17, remove inverted commas from the word “is”.

page 4 line 19, add “Finally a” before “summary”.

page 5 line 17, added “The vertical bin size of ADCP measurements are 1 m for Station A1 and 2 m for other stations.” to the text, and added a new column to Table 1.

page 5 line 26, add “Station” before “A1”.

page 6 line 1, add “According to Rayleigh criterion, to separate P_1 from K_1 and K_2 from S_2 reqires 182.6 days (e. g., Pugh, 1987, p.113), thus”

page 6 line 3-4, “. In the present study” changed to “in this study. Moreover,”.

page 7 line 6, add “The vertical structures of current ellipses of the constituents K_1, O_1, Q_1, M_2, S_2, and N_2 at each station are shown in Fig. 2. It can be seen that there are little vertical changes in the ellipses for all constituents at all stations, except for the top layer where the currents suffer strong disturbances due to winds, at some stations for some constituents. This vertical uniformity indicates that the tidal currents are basically of barotropic nature at all stations. Thus, we only use vertically averaged currents to reveal the characteristics of tidal currents in this study.” to the text, and add Fig. 2.

page 13 line 8, add “DTU10 is the best one in the area between the South China Sea and Java Sea, due to use of more satellites and longer altimeter measurements. Moreover, DTU10 has the highest resolution among these four tide models. It indicates that if the open boundary of a tidal model is located in the area between the South China Sea and Java Sea, DTU10 is the best choice for deriving open boundary condition.” to the text, and add new rows to Table A1.

page 13 line 21, add “Fig. A1 shows the co-tidal charts for K_1, O_1, M_2 and S_2 based on DTU10. For K_1, the tidal waves from the SCS and the JS meet in the study area. For O_1, the tidal wave propagates from the SCS to the JS. For M_2, the tidal wave propagates clockwise around the Belitung Island. For S_2, the tidal wave also propagates clockwise around the Belitung Island, and a clockwise amphidromic system exist near Station A1. K_1 has the largest amplitude (exceeding 0.6 m near the Bangka Island), and then the next is O_1, the amplitudes of M_2 and S_2 are significantly smaller.” to the text, and add Fig. A1.

page 18 line 1, add “Pugh, D.T.: Tides, Surges, and Mean Sea Level. John Wiley & Sons Ltd, 472 pp, 1987.”.

Tidal elevation, current and energy flux in the area between the South China Sea and Java Sea

Zexun Wei[1,2], Guohong Fang[1,2], R. Dwi Susanto[3], Tukul Rameyo Adi[4], Bin Fan[1], Agus Setiawan[4], Shujiang Li[1], Yonggang Wang[1,2], Xiumin Gao[1]

[1]{ The First Institute of Oceanography, State Oceanic Administration, Qingdao, China }

[2]{ Laboratory for Regional Oceanography and Numerical Modeling, Qingdao National Laboratory for Marine Science and Technology, Qingdao, China }

[3]{ Department of Atmospheric and Oceanic Science, University of Maryland, College Park, USA }

[4]{ Agency for Marine & Fisheries Research and Development, Ministry of Marine Affairs and Fisheries, Jakarta, Indonesia }

Correspondence to: Z. X. Wei (weizx@fio.org.cn)

Abstract

The South China Sea (SCS) and the Java Sea (JS) are connected through the Karimata Strait, Gaspar Strait, and the southern Natuna Sea, where the tides are often used as open boundary condition for tidal simulation in the SCS or Indonesian seas. Tides, tidal currents and tidal energy fluxes of the principle constituents K_1, O_1, Q_1, M_2, S_2 and N_2 at five stations in this area have been analyzed using in-situ observational data. The results show that the diurnal tides are the dominant constituents in the entire study area. The constituent K_1 has the largest amplitude, exceeding 50 cm, whereas the amplitudes of M_2 are smaller than 5 cm at all stations. The amplitudes of S_2 may exceed M_2 in Karimata and Gaspar Straits. Tidal currents are mostly of rectilinear type in this area. The major semi-axis lengths of the diurnal tidal current ellipses are about 10 cm s^{-1}, and those of the semi-diurnal tidal currents are smaller than 5 cm s^{-1}. The diurnal tidal energy flows from the SCS to the JS. The semi-diurnal tidal energy flows from the SCS to the JS through the Karimata Strait and the eastern part of the southern Natuna Sea but flows in the opposite direction in the Gaspar Strait and the western part of the southern Natuna Sea. Harmonic analysis of sea level and current observation also

suggest that the study area is located in the anti-nodal~~loop~~ band of the diurnal tidal waves, and in the nodal band of the semi-diurnal tidal waves. Comparisons show that the existing models are basically consistent with the observational results, but further improvements are necessary.

1 Introduction

Tidal system in the Indonesian seas is the most complex one in the world, due to its rugged bottom topography, complicated coastline, and the interference of tidal waves propagating from the Pacific Ocean, Indian Ocean and South China Sea (SCS). The earliest reports of tidal characteristics in the Indonesian seas can be traced back to the colonial period in the early twentieth century, which were recompiled by Wyrtki (1961) to construct diurnal and semidiurnal cotidal charts based on all available coastal and island observations. Although the results of Wyrtki (1961) are impressively reasonable in the Indonesian seas, mapping of the Indonesian tides are still incomplete owing to lack of observations. During the past decades, remarkable progress of investigations about tidal phenomena is benefited by use of satellite altimeter measurements and high resolution numerical simulation, and with no exception in the Indonesian seas. Based on tide gauge observations and TOPEX/Poseidon (T/P) satellite altimeter data, Mazzega and Berge (1994) have produced the cotidal charts of M_2 and K_1 in the Indonesian seas using an inversion method. Using a barotropic tide model, Hatayama et al. (1996) investigated the characteristics of M_2 and K_1 tides and tidal currents in the Indonesian seas, which shows that the tidal currents in the Java Sea (JS) and in the vicinities of narrow straits, i.e. the Lombok and Malacca Strait, are relatively strong.

Egbert and Erofeeva (2002) have assimilated satellite altimeter data into an inverse barotropic ocean tide model, providing the cotidal charts and tidal currents for M_2 and K_1 constituents in the Indonesian seas. Their results are further reported by Ray et al. (2005), showing that there are three types of tides in the Indonesian seas: semidiurnal tides dominated but with significant diurnal inequality in the eastern Indonesian seas and its adjoining region of the Pacific Ocean; mixed diurnal tides in the region west of 118 °E; and diurnal type west of the Kalimantan Island. Using the Regional Ocean Modeling System (ROMS), Robertson and Ffield (2005, 2008) have simulated the barotropic and baroclinic tides in the Indonesian seas for four tidal constituents M_2, S_2, K_1 and O_1. The results show that semidiurnal tides originate from both the Pacific and Indian Oceans; whereas the diurnal tides are mainly from the Pacific Ocean. These results are confirmed by Teng et al. (2013), which suggests that the M_2

tide mainly propagates from the Indian Ocean into the Pacific Ocean through the eastern Indonesian seas, whereas the K_1 and O_1 tides propagate in an opposite direction. Although the characteristics of Indonesian tides have been simulated with more and more accurate geometry, and the results are indeed better than before, the tides in the southern SCS and JS, particularly in the junction region between the SCS and JS, are still not well determined as reflected by the fact that the simulated results are model dependent.

The junction area between the SCS and the JS, comprising the southern Natuna Sea, the Karimata Strait, and the Gaspar Strait, is a throat connecting the SCS and the Indonesian seas (Fig. 1). Furthermore, this area is also the convergent region of tidal waves that propagate from the SCS or the JS (Hatayama et al., 1996). It is worth noting that the simulated tidal currents in this area are discrepant among different models, even when the satellite altimeter data have been assimilated into the models. This is most possibly due to the coarse altimeter track separation (only one ascending track and one descending track pass through this region (Ray et al., 2005)). Therefore, offshore observations are needed to provide a clearer recognition about the Indonesian tides and to assess the existing model results.

In this study, long-term water level and current profile observations at five stations (Fig. 1) are used to investigate the characteristics of tidal elevation, current and energy flux between the SCS and JS. The results are not only important for understanding local dynamics but also useful for the determination of open boundary condition in tidal simulation of the SCS or Indonesian seas. The rest of the paper is organized as follows: Section 2 gives a description of the observed data; Section 3 presents the analyzed results of tides, tidal currents and tidal energy fluxes; Finally a summary and discussion are given in Section 4.

2 Data

The data used in this study were obtained under the trilateral collaborative project 'The South China Sea – Indonesian seas Transport/Exchange (SITE) and Impacts on Seasonal Fish Migration' which was established in 2006 by the First Institute of Oceanography (FIO), State Oceanic Administration, China, the Agency for Marine and Fisheries Research and Development (AMFRD), Ministry of Marine Affairs and Fisheries, Indonesia, and the Lamont-Doherty Earth Observatory (LDEO), Columbia University, USA. The study area of the project was extended to the Sunda Strait in 2008, and the title of the collaborative program was changed to ‘The South China Sea – Indonesian seas Transport/Exchange (SITE) and Dynamics of Sunda and Lombok Straits, and Their Impacts on Seasonal Fish Migration’.

Current and sea level measurements were made from December 2007 to September 2011 in the southern Natuna Sea, Gaspar Strait and Karimata Strait by using Trawl-Resistant Bottom Mounts (TRBMs). The TRBMs were equipped with Acoustic Doppler Current Profilers (ADCPs) and pressure gauges for measuring current profiles and sea levels. The volume, heat, and freshwater transports between the SCS and Indonesian seas have been previously reported by Fang et al. (2010) and Susanto et al. (2013). In the present paper we focus on the tides and tidal currents in the area as shown in the lower panel of Fig. 1. The measurements were conducted along three sections. Section A is located in the southern Natuna Sea between the Bangka Island and Kalimantan Island. Section B1 is in the Gaspar Strait between the Bangka Island and Belitung Island. Section B2 is located in the Karimata Strait between the Belitung Island and Kalimantan Island. The mean water depths of the five TRBM stations labeled A1, A2, B1, B2 and B3 are 36.6, 48.0, 44.2, 42.8 and 49.0 m, respectively (Table 1). The vertical bin size of ADCP measurements are 1 m for Station A1 and 2 m for other stations. The observational lengths of the sea level and current profile vary from 33 to 960 days as listed in Table 2.

3 Analyzed results from observations

3.1 Tides

Based on the observed sea level data, we extract the harmonic constants of six principle tidal constituents K_1, O_1, Q_1, M_2, S_2, and N_2 using the conventional harmonic analysis method developed by Wang and Fang (1981), which is nearly of the same performance as those developed by Foreman (1977) and Pawlowicz et al. (2002). Since the shortest record length is 33 days (current observation at Station A1), the Rayleigh criterion for separating these six constituents is satisfied. According to Rayleigh criterion, to separate P_1 from K_1 and K_2 from S_2 reqires 182.6 days (e. g., Pugh, 1987, p.113), thus t~~T~~he influences of P_1 on K_1 and K_2 on S_2 are corrected through introducing inference quantities (amplitude ratios and phase-lag differences between P_1 and K_1, and between K_2 and S_2) in this study. ~~In the present study~~Moreover, a nearest tidal gauge station at Keppel harbor (103.82 °E, 1.26 °N) was used as an inference station, where the amplitude ratio and phase-lag difference of P_1 versus K_1 are equal to 0.296 and -10° respectively, and those of K_2 versus S_2 are equal to 0.286 and -2° respectively.

The obtained amplitudes and Greenwich phase-lags for the constituents K_1, O_1, Q_1, M_2, S_2, and N_2 at five stations are listed in Table 3. The harmonic constants of P_1 and K_2 can be derived from those of K_1 and S_2, respectively, listed in the table using the inference relations. It can be seen from the table that the constituent K_1 has the largest amplitude, exceeding 50 cm. The second largest amplitude is that of constituent O_1, exceeding 30 cm. For semidiurnal tides, the amplitudes are all smaller than 5 cm for M_2, while they are greater than 5 cm for S_2 at Stations B1, B2 and B3. For all of the five stations, it is found that the amplitudes of diurnal tides are much greater than those of semidiurnal tides, suggesting that diurnal tides are the dominant constituents in this area. Meanwhile, the results also show that the phase-lags of the diurnal tides slightly increase from Section A to Sections B1 and B2. On the contrary, the phase-lags of the semidiurnal tides dramatically increase from the eastern segment of Section A (represented by Station A2) to Section B2, and from Section B1 to the western segment of Section A (represented by Station A1). These results suggest that the study area is located in the ~~loop (~~anti-nodal~~)~~ band of the diurnal tidal waves but in the nodal band of the semidiurnal tidal waves. As a result, the amplitudes of diurnal tides are greater than those of semidiurnal tides, whereas the phase-lags of diurnal tides change less than those of semidiurnal tides. The semidiurnal tidal waves in this area appear as a superposition of the incident waves propagating from the SCS and Indian Ocean (Ray et al., 2005; Teng et al., 2013). These two incident waves happen to have similar intensity and opposite phase, resulting a nodal band here. In contrast to the semidiurnal tides, the diurnal tidal waves in this area appear as a superposition of the incident waves propagating from the SCS and the Pacific Ocean (Ray et al., 2005; Teng et al., 2013). These two incident waves have basically the same phase, resulting in a anti-nodal~~loop~~ band here.

3.2 Tidal currents

The conventional harmonic method is applied to the current data analysis for extracting the harmonic constants of principle tidal constituents, as done in the analysis of tidal elevation in Section 3.1. The vertical structures of current ellipses of the constituents K_1, O_1, Q_1, M_2, S_2, and N_2 at each station are shown in Fig. 2. It can be seen that there are little vertical changes in the ellipses for all constituents at all stations, except for the top layer where the currents suffer strong disturbances due to winds, at some stations for some constituents. This vertical uniformity indicates that the tidal currents are basically of barotropic nature at all stations. Thus, we only use vertically averaged currents to reveal the characteristics of tidal currents in this study. Parameters of the vertically averaged current ellipse, including major and minor semi-axes (W and w), ellipticity (r), Greenwich phase-lag (φ) and direction (λ) of the maximum current speed, are given in Tables 4a–4e. In the tables, signs of the ellipticity represent the sense of the current vector rotation, positive for counterclockwise and negative for clockwise (the term of ellipticity generally refers to the flatness of an ellipse, here it is defined as the ratio of minor axis versus major axis as done in Fang and Ichiye (1983) and Beardsley et al. (2004)). We can see that at Station A1 the tidal currents rotate counterclockwise except N_2. At Station A2 the tidal currents rotate counterclockwise except S_2. At Station B1 the tidal currents rotate counterclockwise except M_2 and N_2. At Station B2 the diurnal tidal currents rotate counterclockwise, the semi-diurnal currents rotate clockwise. At Station B3 the diurnal tidal currents rotate counterclockwise, while the semi-diurnal currents rotate clockwise except N_2. Fig. ~~2~~ 3 shows the current ellipses of K_1, O_1, M_2 and S_2. We can see that all stations show the characteristics of rectilinear tidal currents. The major semi-axis lengths of tidal current ellipses are 10 cm s^{-1} for diurnal constituents K_1 and O_1, with O_1 slightly smaller than K_1 in the most cases. At Station B1, however, which is located in the Gaspar Strait, diurnal tidal currents are significantly increased by the narrowing effect of the strait. In particular, the maximum speed of O_1 can approach to 20 cm/s. The major semi-axis lengths of tidal current ellipses of the semi-diurnal constituents M_2 and S_2 are generally smaller than 5 cm s^{-1} at all stations.

3.3 Tidal energy flux density

The energy flux across a section of unit width is called flux density. For a specific constituent it can be calculated from harmonic constants of tidal elevation and tidal current by the following formula,

$$\left(F_x,\ F_y\right)=\frac{\rho gh}{T}\int_0^T \zeta(u,\ v)dt=\frac{1}{2}\rho ghH\left[U\cos(\xi-G),\ V\cos(\eta-G)\right] \qquad (1)$$

where, $\left(F_x,\ F_y\right)$ are the east and north components of the tidal energy flux density respectively, T the period of the tidal constituent, ρ the water density (taken to be 1021 kg m^{-3} for a temperature of 28 ℃ and a salinity of 33 which are roughly equal to the mean temperature and salinity in the study area), g the gravity acceleration, h the undisturbed water depth, ζ the tidal elevation, $(u,\ v)$ the east and north components of vertically averaged tidal currents, t the time, H and G the amplitude and phase-lag of the tide, $(U,\ V)$ the amplitudes of the east and north components of vertically averaged tidal current, and $(\xi,\ \eta)$ the phase-lags of the corresponding components of tidal current.

Table 5 lists the east component of energy flux density *Fx*, north component of energy flux density *Fy*, magnitude *F*, and direction θ (in degrees measured clockwise from the true north) at Stations A1, A2, B1, B2 and B3 from observed harmonic constants. Moreover, the direction differences between the current major axis and the energy flux vector $\Delta\theta$ are also given in Table 5 (Since the current ellipse has two major semi-axes with opposite directions, in the calculation of $\Delta\theta$ we choose the one that is aligned with the energy flux). Fig. ~~3~~ 4 shows the tidal energy flux densities of the principal diurnal tidal constituents K_1 and O_1 and the principal semi-diurnal tidal constituents M_2 and S_2.

From Table 5 and Fig. ~~3~~4, it is found that for diurnal tides, the tidal energy flows from the SCS to the JS at all stations. Maximum energy flux densities of 11.6 (for K_1) and 14.7 (for O_1) kW m^{-1} appear at Station B1 in the Gaspar Strait. On the other hand, the tidal energy flux for M_2 tide is quite small and flows to the JS only in the eastern passage of the study area, including the Karimata Strait. In the western passage, including the Gaspar Strait, the M_2 tidal energy flows oppositely from the JS to the SCS. But for S_2 tide, the tidal energy flux flows from SCS to JS at all station except B2. In the Indonesian seas, the magnitudes of tidal energy densities may exceed 100 kW m^{-1} (Ray et al., 2005; Teng et al., 2013), thus the energy fluxes in the study area are relatively small. Table 5 shows that direction differences between energy flux and current major axis are generally small. From directions of energy fluxes shown Fig. ~~3~~ 4 we can judge that (1) the southward incident diurnal and S_2 waves from the SCS are slightly stronger than the northward incident diurnal and S_2 waves from the JS; and (2) the southward incident M_2 wave from the SCS is slightly stronger than the northward incident M_2 wave from the JS in the eastern passage, and is slightly weaker than the latter in the western passage. The feature (2) further indicates that the M_2 amphidromic point should be located between the A1 – B1 line and the A2 – B2 line and the amphidromic system should rotate clockwise.

3.4 Tidal elevation gradients

Based on the tidal currents, the gradients of sea surface height can be derived from the shallow water equations, as done by Proudman and Doodson (1924). The equations in the x (positive for eastward) and y (positive for northward) directions are respectively:

$$\frac{\partial u}{\partial t} = fv - g\left(a - \bar{a}\right) - p \qquad (2)$$

$$\frac{\partial v}{\partial t} = -fu - g\left(b - \bar{b}\right) - q \qquad (3)$$

where f is the Coriolis parameter, and $a = \frac{\partial \zeta}{\partial x}$, $\bar{a} = \frac{\partial \bar{\zeta}}{\partial x}$, $b = \frac{\partial \zeta}{\partial y}$, $\bar{b} = \frac{\partial \bar{\zeta}}{\partial y}$ are elevation gradients of tides and equilibrium tides respectively. The vector of (a, b) is called the tidal elevation gradient vector. The equilibrium tide $\bar{\zeta}$ has been adjusted for the earth's elastic response, and is equal to (see e.g., Fang et al., 1999)

$$\begin{cases} \bar{\zeta} = C \sin 2\phi \cos(\omega t + \lambda) & \text{for diurnal tides (}C_{K_1}\text{=0.104 m, }C_{O_1}\text{=0.070 m)} \\ \bar{\zeta} = C \cos^2 \phi \cos(\omega t + 2\lambda) & \text{for semi-diurnal tides (}C_{M_2}\text{=0.168 m, }C_{S_2}\text{=0.078 m)} \end{cases} \qquad (4)$$

where, λ and ϕ are longitude and latitude respectively. In the Eqs. (2) and (3), p and q represent the east and north components of bottom friction:

$$p = \frac{1}{h} C_D \left(u^2 + v^2\right)^{1/2} u \qquad (5)$$

$$q = \frac{1}{h} C_D \left(u^2 + v^2\right)^{1/2} v \qquad (6)$$

where C_D is the drag coefficient and is taken to be 0.0025 in this study. The values of p and q can be obtained by inserting the observed values of u and v into Eqs. (5) and (6) respectively, and can be decomposed into various constituents with frequencies equal to corresponding tidal constituents through harmonic analysis (similar to the analysis of u and v). The amplitudes and phase-lags of the obtained constituents of p (q) are denoted as P and μ (Q and ν), respectively.

For a given constituent with angular speed equal to ω, we have

$$\begin{cases} u = U\cos(\omega t - \xi) = U'\cos\omega t + U''\sin\omega t \\ v = V\cos(\omega t - \eta) = V'\cos\omega t + V''\sin\omega t \\ \zeta = H\cos(\omega t - G) = H'\cos\omega t + H''\sin\omega t \\ \bar{\zeta} = \bar{H}\cos(\omega t - \bar{G}) = \bar{H}'\cos\omega t + \bar{H}''\sin\omega t \\ p = P\cos(\omega t - \mu) = P'\cos\omega t + P''\sin\omega t \\ q = Q\cos(\omega t - \nu) = Q'\cos\omega t + Q''\sin\omega t \end{cases} \tag{7}$$

where, $U' = U\cos\xi$, $U'' = U\sin\xi$ (the rest are similar). Inserting Eq. (7) into Eqs. (2) and (3) yields

$$\begin{cases} A' = \bar{A}' + (-\omega U'' + fV' - P')/g \\ A'' = \bar{A}'' + (\omega U' + fV'' - P'')/g \end{cases} \tag{8}$$

and

$$\begin{cases} B' = \bar{B}' + (-\omega V'' - fU' - Q')/g \\ B'' = \bar{B}'' + (\omega V' - fU'' - Q'')/g \end{cases} \tag{9}$$

where, $\left(A', A'', \bar{A}', \bar{A}''\right) = \frac{\partial}{\partial x}\left(H', H'', \bar{H}', \bar{H}''\right)$, and $\left(B', B'', \bar{B}', \bar{B}''\right) = \frac{\partial}{\partial y}\left(H', H'', \bar{H}', \bar{H}''\right)$. The elevation gradients of equilibrium tides ($\bar{A}', \bar{A}'', \bar{B}', \bar{B}''$) can be obtained from Eq. (4). By inserting $\left(\bar{A}', \bar{A}'', \bar{B}', \bar{B}''\right)$ into Eqs. (8) and (9), we can get the values of the tidal elevation gradients $\left(A', A''; B', B''\right)$. The tidal elevation gradient ellipse parameters can be obtained from the values of $\left(A', A''; B', B''\right)$ in the same way as the calculation of tidal current ellipse parameters from the values of $\left(U', U''; V', V''\right)$. The tidal elevation gradient ellipse has a close relationship to the tidal regime, that is, the distribution of co-amplitude and co-phase-lag contours (see Appendix B for detailed derivation). In particular, if the tidal elevation gradient ellipse rotates counterclockwise (clockwise) the angle from the vector grad *H* to the vector grad *G* on the cotidal chart lies between 0 °and 180 °(0 °and -180 °).

Fig. ~~4~~ 5 shows the tidal elevation gradient ellipses of K_1, O_1, M_2 and S_2 at the observation stations. For K_1 and O_1 tides, the tidal elevation gradient vectors rotate counterclockwise at Stations A1, A2 and B2, and rotate clockwise at Stations B1 and B3. For M_2 tide, the tidal elevation gradient vectors rotate counterclockwise at Stations A1 and A2, and rotate clockwise at Stations B1, B2 and B3. But for S_2 tide, the tidal elevation gradient vectors rotate counterclockwise at Stations A1 and B1, and rotate clockwise at Stations A2, B2 and B3.

From the known tidal elevation gradient we have calculated the directions of the co-tidal and co-amplitude lines as done by Proudman and Doodson (1924) in constructing co-tidal charts of the North Sea. Since the purpose of the present work is not to construct co-tidal charts in the study area, the obtained results are not shown here.

4 Summary and discussion

The sea level and current data obtained at five stations along three sections between the SCS and JS are analyzed to reveal the characteristics of tides and tidal currents in this region. The results show that the ratios of diurnal versus semidiurnal tides amplitudes $(H_{O1}+H_{K1})/(H_{M2}+H_{S2})$ are greater than eight at all stations, suggesting predominance of the diurnal tides in the study area. The amplitudes of K_1 are larger than 50 cm at all stations with the phase-lags being around 30°. In comparison, the amplitudes of M_2 are smaller than 5 cm. It is worth mentioning that the amplitudes of S_2 may exceed M_2 in the Karimata and Gaspar Straits. The greater amplitudes and smaller spatial phase-lag changes of diurnal tides compared with those of semidiurnal tides indicate that the study area is located in the ~~loop~~ ~~(~~anti-nodal~~)~~ band of the diurnal tidal waves but in the nodal band of the semidiurnal tidal waves.

The tidal currents are analyzed based on the ADCP observations on board of 5 TRBMs, showing that the tidal currents are of rectilinear type at all stations. The major semi-axis lengths of tidal current ellipses are about 10 cm s^{-1} for diurnal tides, with O_1 slightly smaller than K_1 in the most cases. But in the Gaspar Strait, O_1 may exceed K_1 and approaches to 20 cm/s at Station B1. The maximum speeds of semi-diurnal constituents M_2 and S_2 are generally smaller than 5 cm s^{-1} at all stations.

By examining the tidal energy fluxes at each station, we found that the diurnal tidal energy flows from the SCS to the JS with the maximum energy flux density of 14.7 kW m^{-1} appearing at Station B1. The tidal energy flux distributions of semidiurnal tides are quite complicated: M_2 energy flux flows southward in the Karimata Strait but northward in the Gaspar Strait; S_2 energy flux generally flows from the SCS to JS except at Station B2.

With these long-term observational results, we can make an accuracy assessment on the existing tidal models for the study area. Four representative tidal models, TPXO7.2 (Egbert and Erofeeva, 2002; 0.25°×0.25° resolution), GOT00.2 (Ray, 1999; 0.5°×0.5°), NAO.99b

(Matsumoto et al., 2000; 0.5 °× 0.5 °), and DTU10 (Cheng and Andersen, 2011; 0.125 °× 0.125 °), are compared with our observations for tides (see appendix A). The comparison shows that the amplitudes and phase-lags of the model results are generally consistent with the observations. However, discrepancies of the model results from the observations are not ignorable. DTU10 is the best one in the area between the South China Sea and Java Sea, due to use of more satellites and longer altimeter measurements. Moreover, DTU10 has the highest resolution among these four tide models. It indicates that if the open boundary of a tidal model is located in the area between the South China Sea and Java Sea, DTU10 is the best choice for deriving open boundary condition. The tidal currents of the model TPXO7.2 are also compared with observations in Appendix A (the models GOT00.2, NAO.99b, and DTU10 do not contain tidal currents). The comparison shows that the relative discrepancies are generally greater than those for tidal elevations. Therefore, further effort of assimilating the in situ observations into numerical model in the future is worthwhile in providing more accurate knowledge of the tidal systems in the study area. Since the study area is often chosen as an open boundary in simulating tides in the SCS or Indonesian seas (e. g., Fang et al., 1999; Gao et al., 2015) the observational results of this study are expected to be useful in improving model results.

Appendix A: Comparison with existing model results

Table A1 shows the comparison of the tidal harmonic constants between observations and the global ocean tide models TPXO7.2 ~~(Egbert and Erofeeva, 2002; 0.25 °× 0.25 ° resolution)~~, GOT00.2 ~~(Ray, 1999; 0.5 °× 0.5 °)~~, NAO.99b ~~(Matsumoto et al., 2000; 0.5 °× 0.5 °)~~ and DTU10 ~~(Cheng and Andersen, 2011; 0.125 °× 0.125 °)~~. Fig. A1 shows the co-tidal charts for K_1, O_1, M_2 and S_2 based on DTU10. For K_1, the tidal waves from the SCS and the JS meet in the study area. For O_1, the tidal wave propagates from the SCS to the JS. For M_2, the tidal wave propagates clockwise around the Belitung Island. For S_2, the tidal wave also propagates clockwise around the Belitung Island, and a clockwise amphidromic system exist near Station A1. K_1 has the largest amplitude (exceeding 0.6 m near the Bangka Island), and then the next is O_1, the amplitudes of M_2 and S_2 are significantly smaller.

Table A2 shows the comparison of the tidal current harmonic constants between observations and TPXO7.2. The Cressman interpolation method (Cressman, 1959) is used here.

Appendix B: Relationship between the rotation of tidal elevation gradient and the tidal regime

The tidal regime for a specific constituent is conventionally illustrated with a diagram, called co-tidal chart, showing its co-amplitude contours and co-phase contours. The tidal elevation of the constituent can be written as

$$\zeta = H\cos(\omega t - G) \qquad \text{(B1)}$$

where H and G are its amplitude and phase-lag respectively, and ω the angular speed. The equivalent complex form of Eq. (B1) is

$$\zeta = \frac{1}{2}H(e^{i(\omega t-G)} + e^{-i(\omega t-G)}) \qquad \text{(B2)}$$

The x and y components of the tidal elevation gradient are

$$a \equiv \frac{\partial\zeta}{\partial x} = \frac{1}{2}\left[\left(\frac{\partial H}{\partial x} - i\frac{H\partial G}{\partial x}\right)e^{i(\omega t-G)} + \left(\frac{\partial H}{\partial x} + i\frac{H\partial G}{\partial x}\right)e^{-i(\omega t-G)}\right] \qquad \text{(B3)}$$

$$b \equiv \frac{\partial\zeta}{\partial y} = \frac{1}{2}\left[\left(\frac{\partial H}{\partial y} - i\frac{H\partial G}{\partial y}\right)e^{i(\omega t-G)} + \left(\frac{\partial H}{\partial y} + i\frac{H\partial G}{\partial y}\right)e^{-i(\omega t-G)}\right] \qquad \text{(B4)}$$

respectively. The gradient vector on the complex plane is thus equal to

$$S = a + ib = \frac{1}{2}\left(Ae^{i(\omega t-G+\alpha)} + Be^{-i(\omega t-G-\beta)}\right) \qquad \text{(B5)}$$

where

$$A = \left\{\left[\left(\frac{\partial H}{\partial x}\right)^2 + \left(\frac{\partial H}{\partial y}\right)^2\right] + \left[\left(\frac{H\partial G}{\partial x}\right)^2 + \left(\frac{H\partial G}{\partial y}\right)^2\right] + 2\left(\frac{\partial H}{\partial x}\frac{H\partial G}{\partial y} - \frac{\partial H}{\partial y}\frac{H\partial G}{\partial x}\right)\right\}^{1/2} \qquad \text{(B6)}$$

$$B = \left\{\left[\left(\frac{\partial H}{\partial x}\right)^2 + \left(\frac{\partial H}{\partial y}\right)^2\right] + \left[\left(\frac{H\partial G}{\partial x}\right)^2 + \left(\frac{H\partial G}{\partial y}\right)^2\right] - 2\left(\frac{\partial H}{\partial x}\frac{H\partial G}{\partial y} - \frac{\partial H}{\partial y}\frac{H\partial G}{\partial x}\right)\right\}^{1/2} \qquad \text{(B7)}$$

$$\alpha = \arctan\left[\left(\frac{\partial H}{\partial y} - \frac{H\partial G}{\partial x}\right)\Big/\left(\frac{\partial H}{\partial x} + \frac{H\partial G}{\partial y}\right)\right] \qquad \text{(B8)}$$

$$\beta = \arctan\left[\left(\frac{\partial H}{\partial y} + \frac{H\partial G}{\partial x}\right)\Big/\left(\frac{\partial H}{\partial x} - \frac{H\partial G}{\partial y}\right)\right] \qquad \text{(B9)}$$

The first term on the right-hand side of Eq. (B5) represents a vector rotating counterclockwise with its tip along a circle of radius A, and the second term represents a vector rotating clockwise with its tip along a circle of radius B. Their sum divided by 2 is the tidal elevation gradient vector S whose tip traces an ellipse, called tidal elevation gradient ellipse. The parameters of the ellipse can be readily derived from A, B, α and β (Godin, 1972, §2.6.1; Fang, 1984):

semimajor axis length = $A + B$ (B10)

ellipticity = $(A - B)/(A + B)$ (B11)

phase-lag of maximum gradient = $G+\frac{1}{2}(\beta - \alpha)$ (B12)

direction of maximum gradient = $\frac{1}{2}(\alpha + \beta)$ (B13)

From Eq. (B5) we can see that the vector S rotates counterclockwise (clockwise) when $A>B$ ($A<B$). From Eqs. (B6) and (B7) the magnitudes of A and B can be further written as

$$A = (|\mathrm{grad}H|^2 + |H\mathrm{grad}G|^2 + 2|\mathrm{grad}H||H\mathrm{grad}G|\sin\psi)^{1/2} \quad \text{(B14)}$$

$$B = (|\mathrm{grad}H|^2 + |H\mathrm{grad}G|^2 - 2|\mathrm{grad}H||H\mathrm{grad}G|\sin\psi)^{1/2} \quad \text{(B15)}$$

where ψ is the angle from the vector grad H to the vector grad G. Therefore, the tidal elevation gradient ellipse becomes a counterclockwise (clockwise) rotating circle if ψ = 90°(-90°); it reduces to a straight line if ψ = 0° or 180°; it rotates counterclockwise (clockwise) if ψ lies between 0° and 180° (0° and -180°). The directions of the vectors grad H and grad G and the angle ψ can be readily obtained from the co-amplitude and co-phase contours in the co-tidal chart.

Acknowledgements

This study was supported by the International Cooperation Program of China (Grant No. 2010DFB23580), the National Basic Research Program of China (973 Program) (Grant No. 2011CB403502), the NSFC-Shandong Joint Fund for Marine Science Research Centers (Grant No. U1406404), the National High Technology Research and Development Program (863 Program) (Grant No. 2013AA09A506), the National Natural Science Foundation of China (Grant Nos. 41476025 and 41306031), the State Oceanic Administration of China (Grant No. 2200207), the Basic Research Operating Funds of the First Institute of Oceanography, State Oceanic Administration (Grant No. 2014G26 and 2013G35), the National Science Foundation of the United States (Grant No. OCE-07-25935), and the Office of Naval Research of the United States (Grant No. N00014-08-1-0618).

References

Beardsley, R. C., Duda, T. F., Lynch, J. F., Irish, J. D., Ramp, S. R., Chiu, C. S., Tang, T. Y., Yang, Y. J., and Fang, G. H.: Barotropic tide in the northeast South China Sea. IEEE J. Oceanic Engineering, 29(4), 1075-1086, 2004.

Cao, D. M., Fang, G. H., Huang, Q. Z., Yu, K. J., and Wang, X. Y.: Tidal regime in the Nansha sea area and its adjacent southwest waters. Oceanologia et Limnologia Sinica, 28(2), 198-208, 1997 (in Chinese with English abstract).

Cheng, Y. C. and Andersen, O. B.: Multimission empirical ocean tide modeling for shallow waters and polar seas. Journal of Geophysical Research, 116, C11001, doi:10.1029/2011JC007172, 2011.

Cressman, G. P.: An operational objective analysis system. Monthly Weather Review, 87(10), 367-374, 1959.

Egbert, G. D. and Erofeeva, S. Y.: Efficient inverse modeling of barotropic ocean tides. Journal of Atmospheric and Oceanic Technology, 19, 183-204, 2002.

Fang, G. H. and Ichiye, T.: On the vertical structure of tidal currents in a homogeneous sea. Geophysical Journal of the Royal Astronomical Society, 73(1), 65-82, 1983.

Fang, G. H.: Basic characteristics of the vertical structure of tidal currents – A comparison of theory and observations. Marine Sciences, 8(3), 1-11, 1984 (in Chinese with English abstract).

Fang, G. H., Kwok, Y. K., Yu, K. J., and Zhu, Y. H.: Numerical simulation of principal tidal constituents in the South China Sea, Gulf of Tonkin and Gulf of Thailand. Continental Shelf Research, 19, 845-869, 1999.

Fang, G. H., Susanto, R. D., Wirasantosa, S., Qiao, F. L., Supangat, A., Fan, B., Wei, Z. X., Sulistiyo, B., and Li, S. J.: Volume, heat, and freshwater transports from the South China Sea to Indonesian seas in the boreal winter of 2007-2008. Journal of Geophysical Research, 115, C12020, doi:10.1029/2010JC006225, 2010.

Foreman, M. G. G.: Manual for tidal heights analysis and prediction. Pacific Marine Science Report 77-10, Institute of Ocean Science, Victoria, B. C., 101 pp, 1977.

Gao, X. M, Wei, Z. X., Lv, X. Q., Wang, Y. G., and Fang G. H.: Numerical study of tidal dynamics in the South China Sea with adjoint method. Ocean Modelling, 92, 101-114, doi:10.1016/j.ocemod.2015.05.010, 2015.

Godin, G.: The Analysis of Tides. University of Toronto Press, Toronto, 264 pp, 1972.

Hatayama, T., Awaji, T., and Akitomo, K.: Tidal currents in the Indonesian seas and their effect on transport and mixing. Journal of Geophysical Research, 101(C5), 12353-12373, 1996.

Matsumoto, K., Takanezawa, T., and Ooe, M.: Ocean tide models developed by assimilating TOPEX/POSEIDON altimeter data into hydrodynamical model: A global model and a regional model around Japan. Journal of Oceanography, 56, 567–581, 2000.

Mazzega, P. and Berge, M.: Ocean tides in the Asian semienclosed seas from TOPEX/POSEIDON. Journal of Geophysical Research, 99(C12), 24867-24881, 1994.

Pawlowicz, R., Beardsley, B., and Lentz, S.: Classical tidal harmonic analysis including error estimates in MATLAB using T_TIDE. Computers and Geosciences, 28(8), 929–937, 2002.

Proudman, J. and Doodson, A. T.: The principal constituent of the tides of the North Sea. Phil. Trans. R. Soc. Lond., A224, 185-219, 1924.

Pugh, D.T.: Tides, Surges, and Mean Sea Level. John Wiley & Sons Ltd, 472 pp, 1987.

Ray, R. D.: A global ocean tide model from TOPEX/POSEIDON altimetry: GOT99.2. NASA/TM-1999-209478, Goddard Space Flight Centre, Greenbelt, MD, USA, 1999.

Ray, R. D., Egbert, G. D., and Erofeeva, S. Y.: A brief overview of tides in the Indonesian seas. Oceanography, 18(4), 74-79, 2005.

Robertson, R. and Ffield, A.: M_2 baroclinic tides in the Indonesian seas. Oceanography, 18(4), 62-73, 2005.

Robertson, R. and Ffield, A.: Baroclinic tides in the Indonesian seas: Tidal fields and comparisons to observations. Journal of Geophysical Research, 113, C07031, doi:10.1029/2007JC004677, 2008.

Susanto, R. D., Wei, Z. X., Adi, R. T., Fan, B., Li, S. J., and Fang, G. H.: Observations of the Karimata Strait througflow from December 2007 to November 2008. Acta Oceanologica Sinica, 32(5), 1–6 , doi:10.1007/s13131-013-0307-3, 2013.

Teng, F., Fang, G. H., Wang, X. Y., Wei, Z. X., and Wang, Y. G.: Numerical simulation of principal tidal constituents in the Indonesian adjacent seas. Advances in Marine Science, 31(2), 166-179, 2013 (in Chinese with English abstract).

Wang, J. and Fang, G. H.: An analysis of incomplete hourly tidal records. Acta Oceanologica Sinica, 3(2), 193-210, 1981 (in Chinese with English abstract).

Wyrtki, K.: Physical oceanography of the Southeast Asian waters, Scientific Results of Marine Investigations of the South China Sea and the Gulf of Thailand 1959-1961. NAGA Rep. 2, 195 pp., Scripps Inst. of Oceanogr., La Jolla, Calif., 1961.

Table 1. Locations and water depths of the observational stations.

Station	Longitude	Latitude	Depth (m)	Bin size (m)
A1	106°50.1' E	1°40.0' S	36.6	1
A2	107°59.2' E	1°05.5' S	48.0	2
B1	107°09.6' E	2°46.8' S	44.2	2
B2	108°15.0' E	2°17.0' S	42.8	2
B3	108°33.0' E	1°54.9' S	49.0	2

带格式表格

Table 2. Record length of the obtained data.

Station	Measuring parameter	Starting and ending dates (yyyy.mm.dd)	Length (d)
A1	Current profile	2008.01.13 - 2008.02.14	33
	Sea level	2008.01.13 - 2008.05.05	114
A2	Current profile	2007.12.04 - 2008.01.12 2008.02.15 - 2008.11.01	301
	Sea level	2007.12.02 - 2008.05.05	156
B1	Current profile	2008.05.12 - 2008.10.11 2008.11.07 - 2008.11.15 2009.10.19 – 2009.10.24	168
	Sea level	2008.05.12 - 2008.11.03	176
B2	Current profile	2008.11.02 - 2010.11.11	740
	Sea level	2009.10.18 - 2010.11.11	390
B3	Current profile	2008.11.07 - 2009.10.17 2009.10.19 – 2010.11.12 2011.02.17 – 2011.09.29	960
	Sea level	2008.11.06 - 2009.09.09	308

Table 3. Tidal harmonic constants at the observation stations.

Constituent	A1		A2		B1		B2		B3	
	H (cm)	*G* (deg)	*H* (cm)	*G* (deg)	*H* (cm)	*G* (deg)	*H* (cm)	*G* (deg)	*H* (cm)	*G* (deg)
K_1	59.1	30.0	50.8	27.0	59.6	33.3	54.4	45.4	57.2	36.2
O_1	42.4	329.1	37.4	326.8	39.6	344.7	36.5	354.7	35.2	343.9
Q_1	7.8	306.1	7.2	305.4	7.4	324.3	7.3	335.0	11.7	339.4
M_2	3.8	341.3	4.4	322.9	4.3	236.4	1.9	117.5	2.2	68.5
S_2	2.6	82.3	2.7	62.2	5.3	160.0	5.6	123.8	8.7	96.5
N_2	0.4	306.6	0.8	284.9	2.0	206.6	0.6	192.6	0.5	8.7

Table 4. Vertically averaged tidal current ellipse.

(a) Station A1

Constituent	W (cm s^{-1})	w (cm s^{-1})	r	φ (deg)	λ (deg)
K_1	9.63	0.70	0.07	136.6/316.6	12.6/192.6
O_1	8.02	3.34	0.42	114.2/294.2	355.2/175.2
Q_1	2.25	0.58	0.26	108.0/288.0	338.0/158.0
M_2	2.34	0.38	0.16	128.9/308.9	153.4/333.4
S_2	1.83	0.16	0.09	92.1/272.1	158.1/338.0
N_2	0.97	0.19	-0.19	113.3/293.3	158.1/338.1

(b) Station A2

Constituent	W (cm s^{-1})	w (cm s^{-1})	r	φ (deg)	λ (deg)
K_1	11.51	1.89	0.16	144.9/324.9	348.8/168.8
O_1	10.31	1.97	0.19	120.3/300.3	339.9/159.9
Q_1	2.41	0.16	0.06	103.4/283.4	335.8/155.8
M_2	3.00	0.58	0.19	8.7/188.7	176.7/356.7
S_2	2.28	0.79	-0.35	18.5/198.5	163.3/343.3
N_2	0.80	0.30	0.37	164.3/344.3	0.2/180.2

(c) Station B1

Constituent	W (cm s^{-1})	w (cm s^{-1})	r	φ (deg)	λ (deg)

K_1	13.32	0.05	0.00	82.4/262.5	167.4/347.4
O_1	19.08	0.77	0.04	13.5/193.5	172.2/352.2
Q_1	4.32	0.39	0.09	162.9/342.9	354.0/174.0
M_2	5.41	1.07	-0.20	89.0/269.0	177.4/357.4
S_2	4.34	0.67	0.16	112.6/292.5	188.0/8.0
N_2	1.40	0.30	-0.21	89.1/269.1	180.7/0.7

(d) Station B2

Constituent	W (cm s^{-1})	w (cm s^{-1})	r	φ (deg)	λ (deg)
K_1	12.25	1.27	0.10	109.7/289.7	119.3/299.3
O_1	11.56	1.55	0.13	25.9/205.9	128.5/308.5
Q_1	2.32	0.36	0.16	169.4/349.4	309.5/129.5
M_2	4.05	0.31	-0.08	37.8/217.8	127.9/307.9
S_2	1.10	0.04	-0.04	157.4/337.4	265.3/85.3
N_2	0.86	0.05	-0.05	5.0/185.0	125.5/305.5

(e) Station B3

Constituent	W (cm s^{-1})	w (cm s^{-1})	r	φ (deg)	λ (deg)
K_1	7.77	0.15	0.02	84.0/264.0	145.5/325.5
O_1	10.26	0.24	0.02	4.8/184.8	146.9/326.9
Q_1	2.25	0.04	0.02	146.4/326.4	327.7/147.7
M_2	4.30	0.06	-0.01	25.1/205.1	144.5/324.5

S_2	1.10	0.40	-0.36	7.8/187.8	116.1/296.1
N_2	0.86	0.08	0.10	178.6/358.6	324.6/144.6

W – length of major semi-axis (i.e. maximum speed); w – length of minor semi-axis (i.e. minimum speed); r – ellipticity, equal to the ratio w/W with signs representing the direction of the current vector rotation (positive/negative for counterclockwise/clockwise); φ – Greenwich phase-lag of the maximum current speed; λ – direction of the major semi-axis measured clockwise from north. Both φ and λ have two values with a difference of 180° respectively.

Table 5. Tidal energy flux density.

(a) Station A1

Constituent	*Fx* (kW m^{-1})	*Fy* (kW m^{-1})	*F* (kW m^{-1})	θ (deg)	$\Delta\theta$ (deg)
K_1	0.0628	-3.0800	3.0806	178.8	-13.8
O_1	1.9216	-5.0011	5.3576	159.0	-16.2
Q_1	0.1394	-0.2759	0.3091	153.2	-4.8
M_2	-0.0746	0.1175	0.1392	327.6	-5.8
S_2	0.0312	-0.0807	0.0865	158.9	0.8
N_2	-0.0023	0.0066	0.0069	340.7	2.6

(b) Station A2

Constituent	*Fx* (kW m^{-1})	*Fy* (kW m^{-1})	*F* (kW m^{-1})	θ (deg)	$\Delta\theta$ (deg)
K_1	3.2910	-6.0846	6.9176	151.6	-17.2
O_1	3.6167	-7.5581	8.3789	154.4	-5.5
Q_1	0.1690	-0.3507	0.3893	154.3	-1.5
M_2	-0.0310	-0.2249	0.2270	187.9	11.2
S_2	-0.0032	-0.1135	0.1135	181.6	18.3
N_2	-0.0050	-0.0079	0.0093	212.6	32.4

(c) Station B1

Constituent	*Fx* (kW m^{-1})	*Fy* (kW m^{-1})	*F* (kW m^{-1})	θ (deg)	$\Delta\theta$ (deg)

K_1	2.4623	-11.2900	11.5554	167.7	0.3
O_1	1.6738	-14.6383	14.7337	173.5	1.3
Q_1	0.0506	-0.6735	0.6754	175.7	1.7
M_2	-0.0752	0.4329	0.4394	350.1	-7.3
S_2	0.0098	-0.3511	0.3512	178.4	-9.6
N_2	-0.0115	0.0289	0.0311	338.3	-22.4

(d) Station B2

Constituent	*Fx* (kW m^{-1})	*Fy* (kW m^{-1})	*F* (kW m^{-1})	θ (deg)	$\Delta\theta$ (deg)
K_1	4.7790	-4.2226	6.3772	131.5	12.2
O_1	5.6926	-5.3376	7.8035	133.2	4.7
Q_1	0.2630	-0.2354	0.3530	131.8	2.3
M_2	0.0157	-0.0282	0.0323	150.8	22.9
S_2	-0.1103	-0.0120	0.1109	263.8	-1.5
N_2	-0.0089	0.0065	0.0110	305.9	0.4

(e) Station B3

Constituent	*Fx* (kW m^{-1})	*Fy* (kW m^{-1})	*F* (kW m^{-1})	θ (deg)	$\Delta\theta$ (deg)
K_1	4.0403	-6.1473	7.3562	146.7	1.2
O_1	4.4794	-7.0172	8.3251	147.4	0.5
Q_1	0.3395	-0.5330	0.6319	147.5	-0.2
M_2	0.0966	-0.1394	0.1696	145.3	0.8

S_2	-0.0328	-0.0787	0.0853	202.6	86.5
N_2	0.0062	-0.0084	0.0104	143.7	-0.9

Fx – east component of energy flux density; *Fy* – north component of energy flux density; *F* – magnitude of energy flux density; θ – direction of energy flux density, measured clockwise from north; $\Delta\theta$ – direction of energy flux density, measured clockwise from the major axis of the current ellipse ($= \theta - \lambda$).

Table A1. Comparison between four tidal models and observations.

Station	Source	K_1			O_1			M_2			S_2		
		H (cm)	*G* (deg)	△ (cm)	*H* (cm)	*G* (deg)	△ (cm)	*H* (cm)	*G* (deg)	△ (cm)	*H* (cm)	*G* (deg)	△ (cm)
	TPXO7.2	66.7	23.0	10.8	45.2	323.9	4.9	5.4	18.0	3.3	1.7	123.9	1.7
	GOT00.2	61.5	26.5	4.4	42.0	325.3	2.8	6.4	357.5	2.9	3.0	93.6	0.7
A1	NAO.99b	56.6	25.5	5.2	41.5	325.6	2.7	4.4	339.1	0.6	0.9	168.1	2.7
	DTU10	59.0	26.8	3.3	41.4	328.6	1.1	4.8	346.4	1.1	0.6	53.4	2.1
	observation	59.1	30.0		42.4	329.1		3.8	341.3		2.6	82.3	
	TPXO7.2	51.0	28.1	1.0	38.3	325.2	1.4	7.6	314.3	3.3	2.3	8.8	2.3
	GOT00.2	53.4	24.3	3.6	37.8	323.8	2.0	5.7	325.6	1.3	0.5	135.3	2.6
A2	NAO.99b	50.8	22.8	3.7	37.4	322.2	3.0	7.3	305.3	3.4	0.2	216.1	2.9
	DTU10	52.6	24.5	2.9	38.4	327.2	1.0	5.4	318.4	1.1	1.6	40.2	1.4
	observation	50.8	27.0		37.4	326.8		4.4	322.9		2.7	62.2	
B1	TPXO7.2	64.6	43.8	12.4	40.3	348.0	2.4	1.8	235.7	2.5	3.6	159.1	1.7

	GOT00.2	61.5	30.5	3.5	36.6	337.5	5.6	1.0	285.1	3.7	4.8	156.0	0.6
	NAO.99b	61.8	30.8	3.4	40.3	337.5	5.1	4.0	231.6	0.5	7.9	190.4	4.3
	DTU10	59.8	33.4	0.2	37.4	343.1	2.4	4.2	254.6	1.3	6.1	178.8	2.0
	observation	59.6	33.3		39.6	344.7		4.3	236.4		5.3	160.0	
	TPXO7.2	55.3	34.2	10.7	38.1	338.0	10.9	2.8	13.2	3.8	3.5	97.6	2.9
	GOT00.2	54.4	27.8	16.6	35.3	335.3	12.2	2.6	93.1	1.2	5.4	146.5	2.2
B2	NAO.99b	52.5	30.3	14.2	35.9	337.1	11.1	4.2	9.7	5.1	2.7	19.5	6.8
	DTU10	55.0	31.0	13.7	37.9	339.5	9.9	2.2	76.9	1.4	4.0	94.1	2.9
	observation	54.4	45.4		36.5	354.7		1.9	117.5		5.6	123.8	
	TPXO7.2	51.8	34.6	5.6	36.6	337.8	4.1	2.2	3.3	2.4	3.2	85.8	5.6
	GOT00.2	54.3	27.4	9.0	35.3	335.3	5.3	2.0	69.3	0.2	5.2	146.7	6.7
B3	NAO.99b	53.7	30.1	6.9	36.8	335.3	5.6	6.6	353.1	6.4	4.5	8.0	9.7
	DTU10	54.6	30.1	6.5	37.9	338.4	4.4	2.3	63.5	0.2	4.5	97.1	4.2
	observation	57.2	36.2		35.2	343.9		2.2	68.5		8.7	96.5	
Average	TPXO7.2			8.10			4.74			3.06			2.84

GOT00.2	7.42	5.58	1.86	2.56
NAO.99b	6.68	5.50	3.20	5.28
DTU10	5.32	3.76	1.02	2.52

$\Delta = \left[(H_m \cos G_m - H_o \cos G_o)^2 + (H_m \sin G_m - H_o \sin G_o)^2 \right]^{1/2}$ is the vector difference, with subscripts m and o representing model and observation respectively.

Table A2. Comparison between TPXO7.2 tidal currents and observations.

Station	Source	K_1					O_1					M_2					S_2				
		U (cm/s)	ξ (deg)	V (cm/s)	η (deg)	△ (cm/s)	U (cm/s)	ξ (deg)	V (cm/s)	η (deg)	△ (cm/s)	U (cm/s)	ξ (deg)	V (cm/s)	η (deg)	△ (cm/s)	U (cm/s)	ξ (deg)	V (cm/s)	η (deg)	△ (cm/s)
A1	TPXO7.2	8.2	25.1	19.7	143.0	13.5	4.5	322.6	11.8	86.5	6.7	3.3	160.3	1.6	13.2	3.1	0.7	244.3	1.0	229.6	1.7
	observation	2.2	118.5	9.4	137.5		3.4	12.8	8.0	112.2		1.1	146.7	2.1	304.3		0.7	104.1	1.7	270.1	
A2	TPXO7.2	5.3	23.5	13.7	120.5	6.1	3.2	311.4	9.0	74.0	6.9	2.1	175.1	2.8	142.2	3.2	0.9	255.6	1.8	201.5	1.2
	observation	2.9	4.5	11.3	143.0		4.0	327.8	9.7	116.3		0.6	82.0	3.0	188.1		1.0	329.4	2.2	204.4	
B1	TPXO7.2	5.9	158.8	9.0	180.9	15.8	3.6	114.5	6.2	146.1	16.0	2.1	311.0	4.1	310.8	4.0	0.7	318.5	1.1	323.3	3.5
	observation	2.9	83.5	13.0	262.4		2.7	30.0	18.9	193.2		1.1	12.0	5.4	269.5		0.9	244.7	4.3	293.8	
B2	TPXO7.2	9.5	87.6	2.2	206.1	7.4	5.6	21.1	1.8	159.6	7.0	1.2	1.3	1.4	179.2	2.9	0.8	295.1	0.7	212.7	1.0
	observation	10.7	113.0	6.1	279.2		9.1	32.0	7.3	196.3		3.2	34.4	2.5	223.5		1.1	337.6	0.1	311.5	
B3	TPXO7.2	8.9	75.1	2.2	237.7	6.5	6.3	360.0	2.4	163.0	6.5	2.6	31.2	2.6	180.8	1.6	0.7	359.0	1.0	215.3	0.5
	observation	4.4	85.6	6.4	263.3		5.6	6.8	8.6	183.9		2.5	23.9	3.5	205.7		1.0	357.7	0.6	224.2	

$$\Delta = \left[(U_m \cos\xi_m - U_o \cos\xi_o)^2 + (U_m \sin\xi_m - U_o \sin\xi_o)^2 + (V_m \cos\eta_m - V_o \cos\eta_o)^2 + (V_m \sin\eta_m - V_o \sin\eta_o)^2 \right]^{1/2}$$

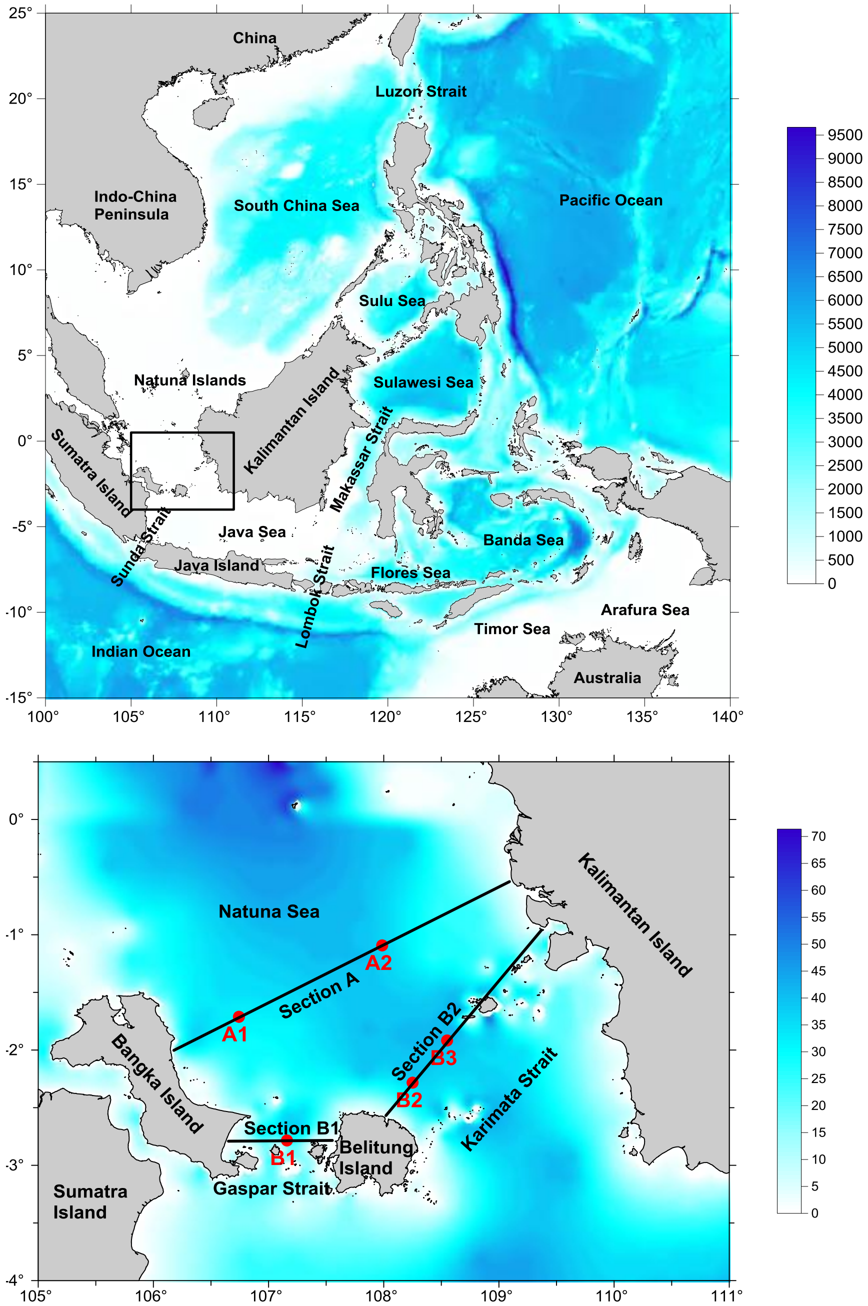

Figure 1. The map of the Indonesian seas (upper), and observational stations (lower). Isobaths are in meters.

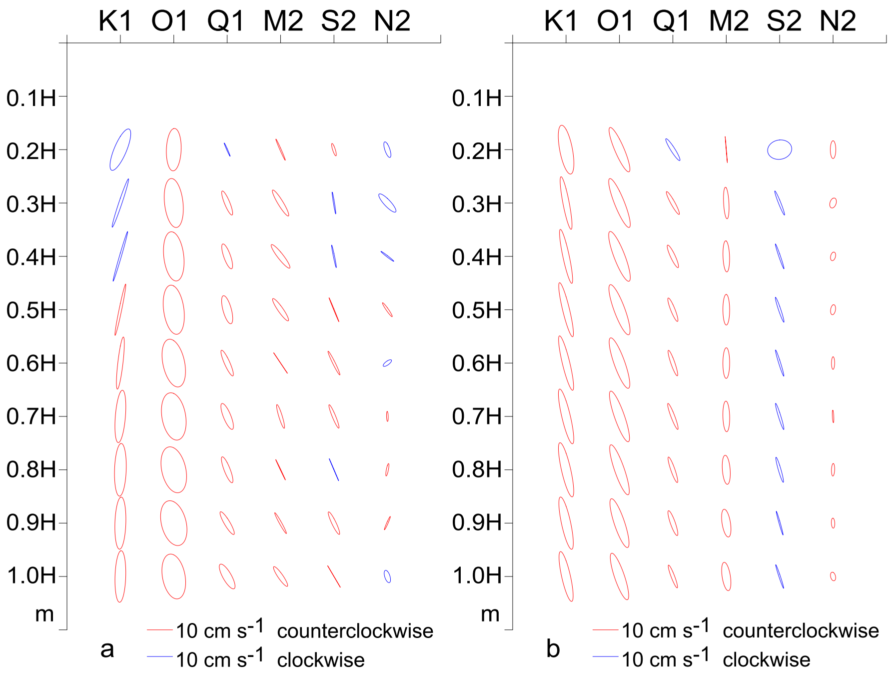

带格式的：字体颜色：自动设置

带格式的：字体颜色：自动设置

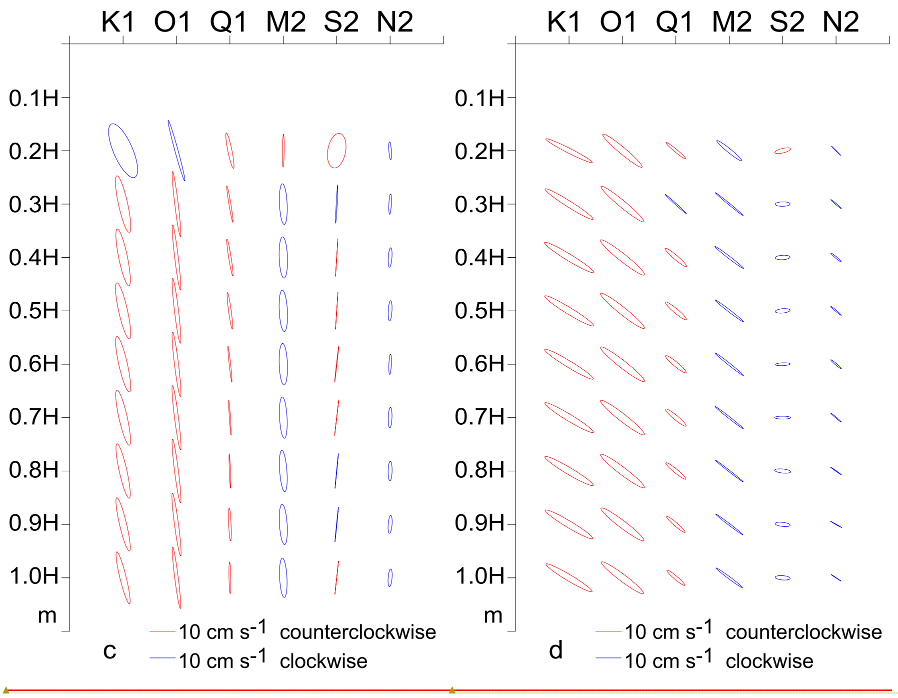

带格式的：字体颜色：自动设置

带格式的：字体颜色：自动设置

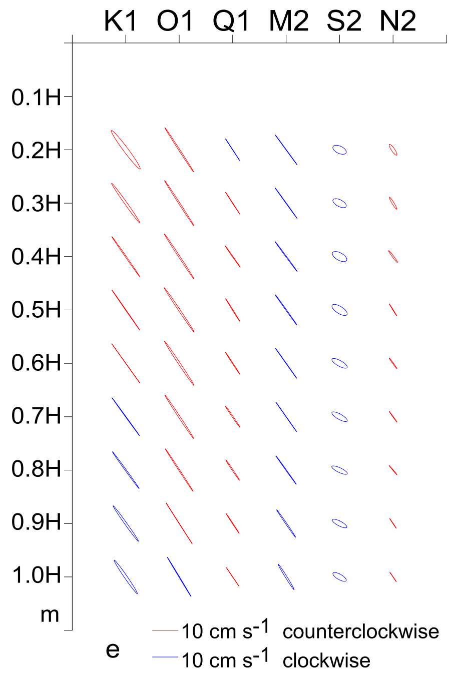

Figure 2. The vertical distributions of current ellipses of tides constituents K_1, O_1, Q_1, M_2, S_2, and N_2 at Stations A1(a), A2(b), B1(c), B2(d) and B3(e).

带格式的：字体颜色：自动设置

带格式的：德语(德国)

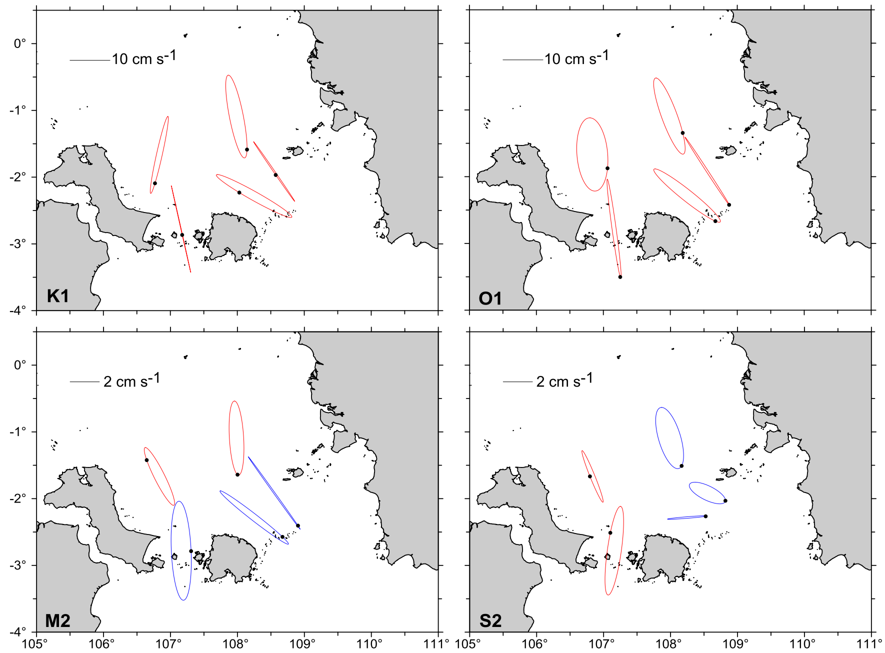

Figure ~~2~~3. The vertically averaged tidal current ellipses of principle tidal constituents K_1, O_1, M_2 and S_2 at the observational stations. Red/blue color indicates counterclockwise/clockwise rotation. Dots on the ellipses represent the tips of the tidal current vectors at zero o'clock GMT.

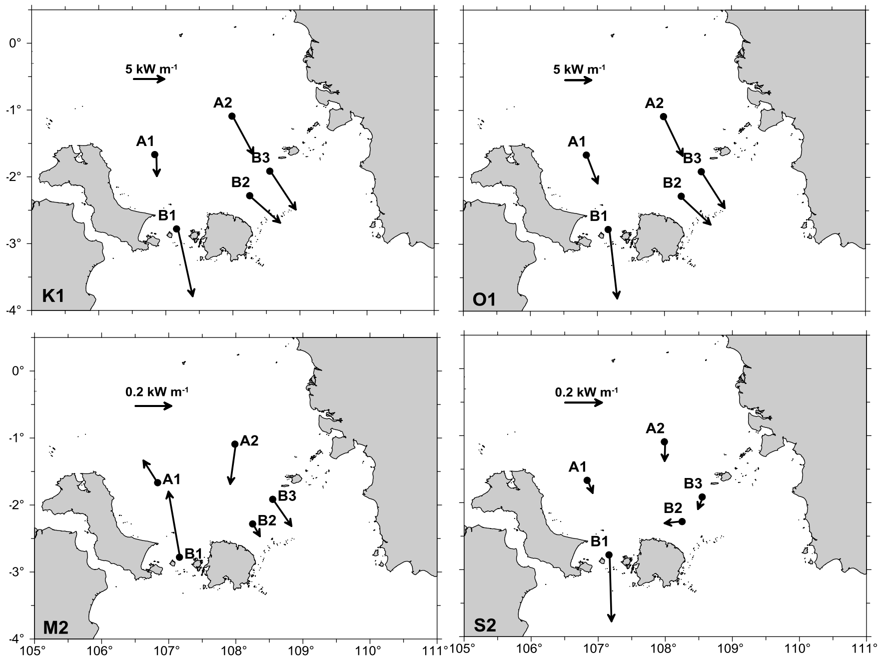

Figure ~~3~~4. Horizontal tidal energy flux density.

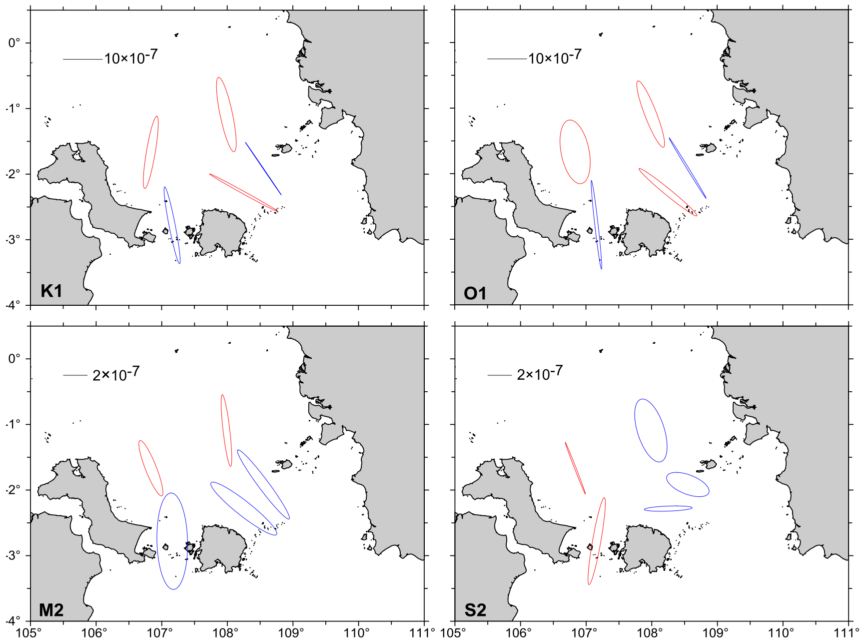

Figure ~~4~~5. The tidal elevation gradient ellipses of K_1, O_1, M_2 and S_2 at the observational stations. Red/blue color indicates counterclockwise/clockwise rotation.

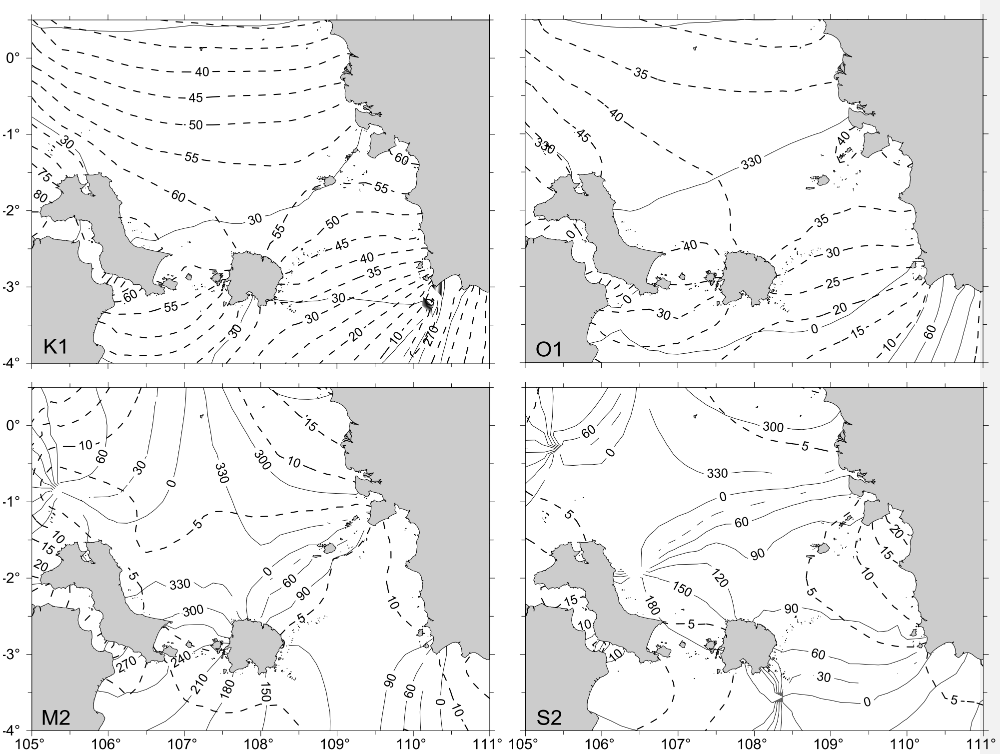

Figure A1. Co-tidal charts for K_1, O_1, M_2 and S_2 based on DTU10 (Dashed line: amplitude (cm), solid line: phase-lag (°)).